1. SCIENTIFIC RESEARCH

CONDENSED MATTER PHYSICS

The main objectives of research in the framework of the theme involved the application of neutron scattering techniques and complementary methods to investigate the structure, dynamics and microscopic properties of nanosystems and novel materials, which are of great importance for the development of nanotechnologies in the fields of electronics, pharmacology, medicine, chemistry, modern condensed matter physics and interdisciplinary sciences.

The greater part of experimental research was carried out on spectrometers of the modernized IBR-2 reactor in accordance with the Topical Plan for JINR Research and International Cooperation and FLNP User Program. A number of scientific experiments were performed in neutron and synchrotron centers in Russia and abroad under the existing cooperation agreements and accepted beam time application proposals. Also, the activities on the modernization of the available spectrometers and the development of new instruments were carried out in accordance with the development program plan for the IBR-2 spectrometers. Most attention was given to the realization of the top-priority projects (construction of a new DN-6 diffractometer for studying microsamples and a multipurpose GRAINS reflectometer).

Within the framework of investigations under the theme the employees of the FLNP Department of Neutron Investigations of Condensed Matter (NICM) maintained broad cooperation with many scientific organizations in Russia and abroad. The cooperation, as a rule, was documented by joint protocols or agreements. In Russia, especially active collaboration was with the thematically-close organizations, such as RRC KI, PNPI, SSC RF IPPE, MSU, IMP UB RAS, IC RAS, INR RAS and others.

A list of the main scientific topics studied by the employees of the NICM Department includes:

- Investigation of structure and properties of novel crystal materials and nanosystems by neutron diffraction;
- Investigation of magnetic colloidal systems in bulk and at interfaces;
- Investigation of structure of carbon nanomaterials;
- Magnetism of layer nanostructures;
- Investigation of nano-scale structure and functional characteristics of biological, colloidal and polymeric nanodispersed materials;
- Investigation of nanostructure and properties of lipid membranes and lipid complexes;
- Investigation of atomic dynamics of nanosystems and materials by neutron inelastic scattering;
- Investigation of texture and properties of minerals and rocks;
- Analysis of internal stresses in bulky materials and factory-made goods.

I. Scientific results

Structure investigations of novel oxide, intermetallic and nanostructured materials

The structural, magnetic, and vibrational properties of $PbFe_{0.5}Nb_{0.5}O_3$ relaxor multiferroic were studied by means of x-ray, neutron diffraction, and Raman spectroscopy at pressures up to 30 GPa in a temperature range from 10 to 300 K [1] (**Fig. 1**). With increasing pressure in a given compound two successive structural phase transitions from the initial R3m rhombohedral polar phase to Cm and Pm monoclinic polar phases were observed at P = 5.5 and 8.5 GPa, respectively. The G-type antiferromagnetic order remains stable in the pressure range under study and the Néel temperature increases with a pressure coefficient $(1/T_N)dT_N/dP$ = 0.012 GPa^{-1}. The existence of high-pressure polar phases in combination with the magnetic order characterized by an increase in T_N in $PbFe_{0.5}Nb_{0.5}O_3$ implies the stability of the magnetoelectric effect and is a unique phenomenon, which is in drastic contrast with a general tendency towards a suppression of polar phases and/or magnetoelectric coupling in the majority of conventional oxide multiferroics under pressure.

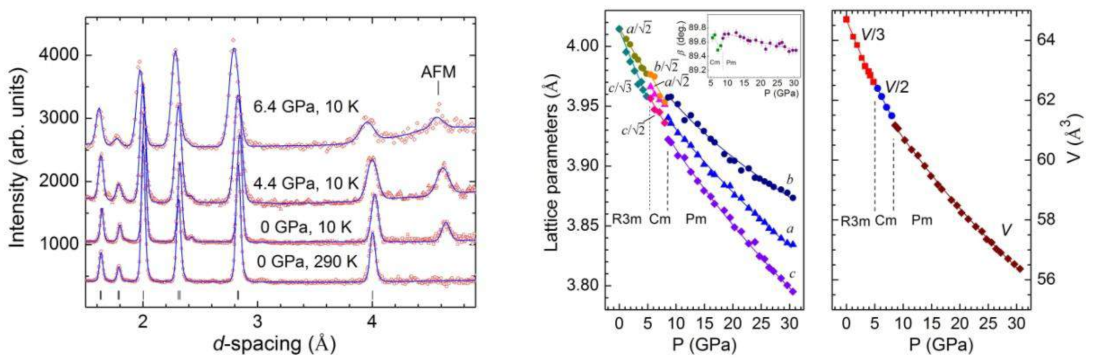

Fig. 1. Neutron diffraction patterns of $PbFe_{0.5}Nb_{0.5}O_3$ (DN-12 diffractometer, IBR-2) measured under high pressures of up to 6.4 GPa and at temperatures of 10 and 290 K (left). The most intense magnetic peak is marked as AFM. The pressure dependencies of lattice parameters and unit cell volume of different phases of $PbFe_{0.5}Nb_{0.5}O_3$ obtained in X-ray diffraction experiments in a wide pressure range of up to 30 GPa (right).

The atomic and magnetic structures of intermetallic cobalt compounds RCo_2 were studied using neutron diffraction in the range of high pressures of 0-4 GPa and temperatures of 10-300 K [2, 3]. For many years these compounds have been considered as model systems demonstrating a phenomenon of itinerant electron metamagnetism (IEM). This phenomenon involves the appearance of transition metal sublattice magnetization as a response to the action of the magnetic field of the rare-earth metal sublattice in intermetallic compounds. In the course of the experiments it was found that the concept of IEM is valid for compounds with sufficiently high magnetic ordering temperatures T_C ~ 150-200 K (R = Tb, Ho), but it cannot describe the magnetic properties of compounds with low values of T_C ~ 30-40 K. Using $ErCo_2$ as an example, the inconsistent behavior of Er and Co sublattice magnetizations and the suppression of Co sublattice magnetism were demonstrated at stable magnetic properties of the Er sublattice under pressure (**Fig. 2**). The obtained results in combination with the theoretical calculations call for further refinement of the IEM concept taking into account the peculiarities of the electronic structure of RCo_2 compounds.

The structural features of promising high-voltage cathode materials based on $LiNi_{0.5}Mn_{1.5}O_4$ - $LiNi_{0.5-x}Mn_{1.5-y}M_{x+y}O_4$ (M = Co, Cr, Ti, Al, Mg; x + y = 0.05), synthesized in the Institute of Chemistry and Mechanochemistry, Siberian Branch of the Russian Academy of Sciences (Novosibirsk) were investigated in order to improve the electrochemical properties of these materials. The unsubstituted $LiNi_{0.5}Mn_{1.5}O_4$ has a high electrochemical potential (4.7 V) corresponding to a flat plateau in the charge-discharge curve at a mean capacity of 120 mAh/g, which significantly increases specific stored energy of the battery as compared to other materials ($LiCoO_2$ ~ 3.8 V, $LiFePO_4$ ~ 3.2 V at the same capacity). Depending on the method of synthesis, $LiNi_{0.5}Mn_{1.5}O_4$ can have either a primitive cubic structure, symmetry $P4_332$, with an ordered arrangement of cations (temperature of synthesis does not exceed 700°C) or face-centered cubic structure, symmetry Fd-3m, with a disordered arrangement of cations (temperatures of synthesis are above 800°C). Because of structural transformations during the cycling the compound $LiNi_{0.5}Mn_{1.5}O_4$ with the space group $P4_332$ shows worse electrochemical behavior as compared to $LiNi_{0.5}Mn_{1.5}O_4$ with the structure Fd-3m.

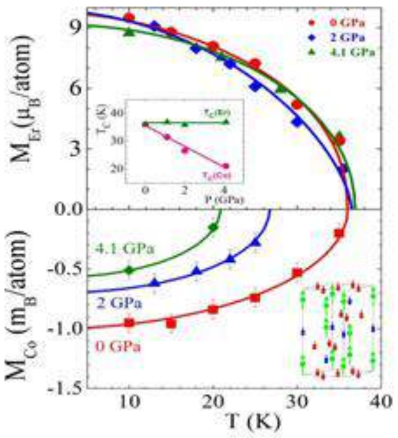

Fig. 2. Temperature dependences of Er and Co sublattice magnetizations in $ErCo_2$ at different pressures, illustrating their independent behavior which is beyond the IEM concept. The insets show the pressure dependences of the Curie temperatures of Er and Co sublattices and the character of the magnetic ordering in these compounds.

The samples under study were synthesized at T < 800°C by means of a small substitution of transition metals for Ni and Mn cations, as well as by using the mechanoactivation procedure for the reactant mixture in a planetary mill. As a result of the treatment of the neutron diffraction spectra using the Rietveld method it was found that all the samples have a two-phase structure. The main phase is the Fd-3m phase, and the extra phase $P4_332$ comprises from 1 to 20% depending on the added metal and the temperature of synthesis. It was observed that the ions of the added metal preferably occupy positions of Ni, which in turn causes the formation of the impurity phase NiO in small amounts (1-2%). The average size of the blocks was 70-80 nm for the samples synthesized at 700°C, and 100-150 nm for the samples synthesized at 800°C. Large microstrains were found mostly, as expected, in the samples with the lower temperature of synthesis.

Investigations of magnetic fluids and nanoparticles

The study of the influence of magnetic nanoparticle loading on the structure of the protein shell in magnetoferritin (synthetic biological complex of apoferritin with different content of magnetic material in the protein cavity) was continued for a wide range of loading factor LF (the number of iron atoms per complex) of the magnetic material [4, 5]. The increase in the magnetic loading up to LF = 910 leads to the loss of solution stability and partial sedimentation. At the same time the small-angle neutron scattering (SANS) from the supernatant solution has a form typical for pure appoferritin (**Fig. 3a**). The results of the experiments on contrast variation (**Fig. 3b**) showed a shift in the effective match point of the complex with increasing LF and growth of the residual scattering in it, which is associated with an increase in the structural polydispersity of the system. As a result, there is a considerably greater (in comparison with the expected value) volume fraction of the magnetic material in the complex, which increases with the loading factor growth, thus pointing to a partial destruction of the apoferritin shell. The work has been done in collaboration with the Institute of Experimental Physics, Slovak Academy of Sciences (Kosice, Slovakia) and the Faculty of Physics of the Taras Shevchenko National University of Kiev (Kiev, Ukraine).

As a part of a comprehensive study of the nanoparticle impact on biological macromolecules in solutions, the data of small-angle scattering of synchrotron radiation (SAXS) for mixtures of fibrillar amyloid protein aggregates of lysozyme (egg white) with magnetoferritin were analyzed. It was revealed from SAXS experiments (**Fig. 4**) and fluorescence analysis that the addition of magnetoferritin to amyloid solutions of lysozyme reduces the amyloid aggregation of proteins [6].

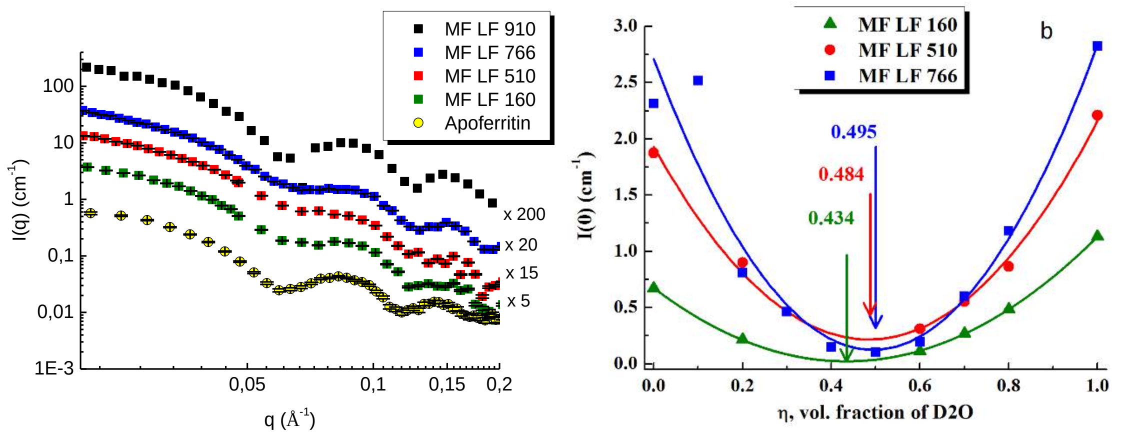

Fig. 3. SANS data for solutions of apoferritin and magnetoferritin with varying load (a). Results of experiments on contrast variation for magnetoferritin with different loading factor (b).

The pair distance distribution functions (**Fig. 4**) obtained using SAXS data strongly suggest the reduction in the size of amyloid aggregates in the mixture with the magnetoferritin complex. The effect was found to be more pronounced for larger loads of the magnetic material. The work has been done in collaboration with the Institute of Experimental Physics, Slovak Academy of Sciences (Kosice, Slovakia), Helmholtz Research Centre Geesthacht (Geesthacht, Germany) and the Faculty of Physics of the Taras Shevchenko National University of Kiev (Kiev, Ukraine).

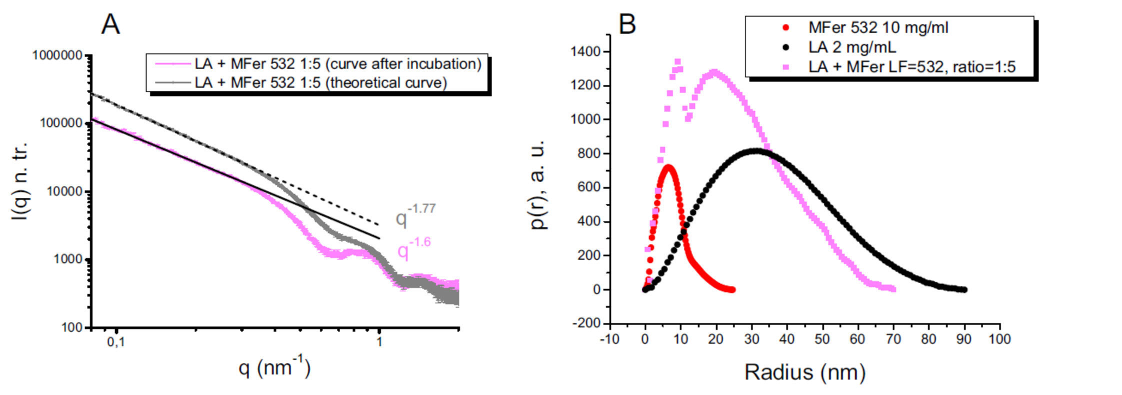

Fig. 4. (A) The experimental scattering curve for a mixture of lysozyme amyloids and magnetoferritin with LF = 532 is compared with the theoretical curve based on the scattering from unmixed solutions. (B) The corresponding pair distance distribution function for the mixture is compared with the similar functions for neat solutions of amyloids and magnetoferritin.

A detailed study of aqueous micellar solutions of sodium oleate and its mixtures with polyethylene glycol PEG (PEG) was carried out within the investigations of the structural reorganization effects previously detected in aqueous magnetic fluids stabilized by sodium oleate on addition of the polymer as a biocompatibiity enhancement component. The SANS data revealed changes in the structure and interactions between the micelles of sodium oleate. The neat aqueous solutions of sodium oleate showed a typical behavior for the solutions of charged micelles characterized by the transition from spherical to cylindrical micelles at 2% surfactant content in the system. The structural parameters of micelles and micellar interaction in solutions of sodium oleate with and without PEG in the system were obtained. The addition of a small (about 2%) amount of

PEG resulted in a decrease in the micelle aggregation number and changes in the degree of aggregation with growing surfactant concentration in the solution. At a high (10%) content of PEG some kind of screening of the intermicellar interaction in the system was observed, presumably due to the effective micelle surface coating by the polymer [7]. The work has been performed in collaboration with Helmholtz Research Centre Geesthacht (Geesthacht, Germany), Institute of Experimental Physics, Slovak Academy of Sciences (Kosice, Slovakia) and the Faculty of Physics of the Taras Shevchenko National University of Kiev (Kiev, Ukraine).

Investigations of carbon nanomaterials

In the framework of research for developing synthesis of biologically active fullerene derivatives, integrated studies (atomic force microscopy, small-angle neutron scattering and infrared spectroscopy) were carried out on aqueous colloidal C60 solutions produced by different methods. It was shown that along with C60 monomers (size of about 0.7 nm) spherical aggregates in a broad size range of 2-50 nm were present in the solutions. The size characteristics (radius of gyration and maximum size) of the aggregates in bulk solutions of three- and six-month age were derived from the SANS data analysis (**Fig. 5**) and were in good agreement with the AFM data obtained for the dried samples. To identify possible additional bonds in the aqueous fullerene solutions, experiments on infrared spectroscopy were performed. The spectra revealed additional peaks that correspond to O-H, C-OH and C-O bonds. This fact indicates that a hydroxyl shell exists on the surface of the fullerene clusters providing for the solution stabilization [8]. The work has been done in collaboration with the Taras Shevchenko National University of Kiev (Kiev, Ukraine).

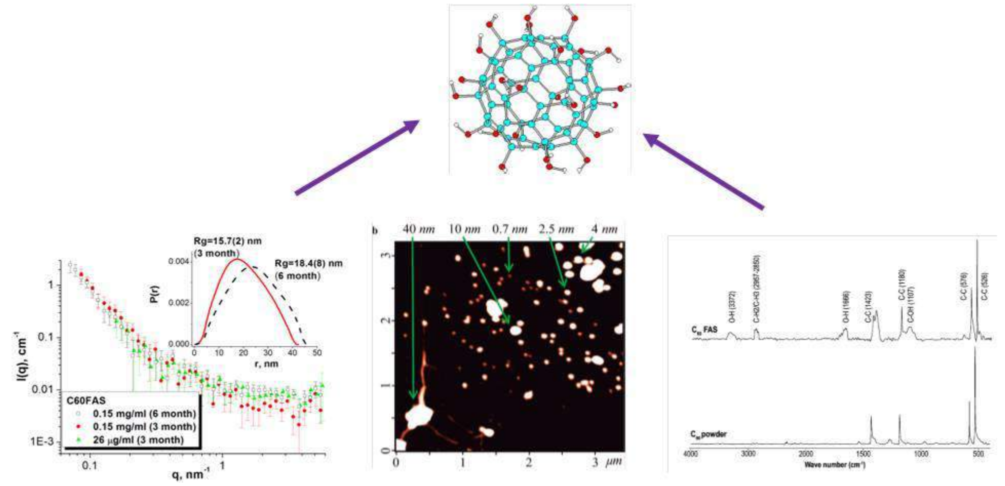

Fig. 5. The proposed model for stabilization of fullerene molecules in water according to the results of the experiments (SANS, AFM and infrared microscopy).

A general theory of small-angle scattering from spherical nanoparticles with a diffuse surface was developed and tested in practice [9] within the framework of structural studies of nanodiamonds. The approximation of low diffusivity and a large width of the diffusive layer, which are observed in SANS experiments on detonation nanodiamonds, was considered. The expressions for the parameters of the particle size distribution function in the lognormal approximation were derived. The dependences of the scattering invariants as a function of the solvent scattering length density in the contrast variation experiments on liquid dispersions of such particles were studied. The theoretical results were used in the analysis of the SANS data on cluster solutions of detonation nanodiamonds in water and dimethylsulfoxide from different manufacturers. Full agreement with the predicted behavior of the scattering invariants with the contrast changes was obtained. The presence of a transitional diamond-graphite region in detonation nanodiamonds in the form of a specific power-law dependence for the average radial density was confirmed. The work has been performed in collaboration with the Ioffe Physical-Technical Institute (St. Petersburg, Russia), Helmholtz Research Centre Geesthacht (Geesthacht, Germany), Nanocarbon Research Institute (Nagano, Japan) and Faculty of Physics of Taras Shevchenko National University of Kiev (Kiev, Ukraine).

The modeling of the kinetics of cluster formation and growth in C60 fullerene solutions was continued. In the extrapolation of numerical solutions of the kinetic equations over time, first estimates of the time evolution of the cluster size distribution function $f(R, t)$ were obtained for a polar saturated solution of C60 (time interval of seven days). Using these data the SANS curves for the solution after various time intervals were calculated. It was shown that according to the model calculations the maximum SANS intensity is observed for the interval ranging from several hours to one day after the solution preparation (**Fig. 6**). The accuracy of the estimates and possibilities of making more accurate calculations for concrete systems are under discussion. The prospects of these studies are linked to the use of new equations including the population balance equation (PBE) method. For the application of this approach, the solution of the model problems was extended to longer periods of the evolution time of the system by using the dynamic grid sampling. In addition to the cases of pure decay and pure particle aggregation we considered a model that takes into account both processes; as the initial interaction "cores" the mathematically simple cores (constant, summation and others) were used.

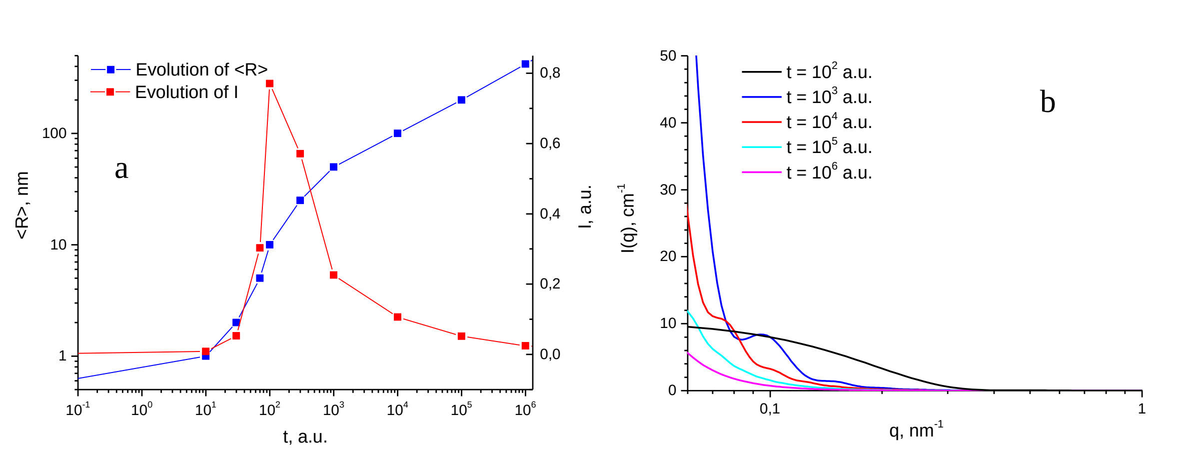

Fig. 6. (a) Model evolution of the average cluster size and average SANS intensity for a polar fullerene solution. (b) Examples of calculated SANS spectra from the cluster size distribution function for the time intervals ranging from several hours to one day after solution preparation.

Investigations of layered nanostructures

On the REMUR reflectometer the nonreciprocal transmission of neutrons through a noncoplanar magnetic system (NCMS) was investigated [10]. The new generation of spintronics elements is based on complex noncoplanar magnetic systems (NCMS), in which the spatial dependence of three orthogonal components of the magnetic field induction takes place. Neutrons, like electrons, have spin s = 1/2, therefore the investigation of neutron transmission processes is of importance for the identification of common features inherent in both kinds of particles. The approximation of the electron-type behavior by neutrons is justified in ferromagnets, where the exchange field is large and the Lorentz force can be neglected. A noncoplanar magnetic system, in accordance with the solution of the Schrödinger equation, is characterized by the properties, which are not inherent in a coplanar magnetic system (CMS), namely, the dependence of the transmission of unpolarized neutrons (or electrons) on the direction of their propagation. To verify this result, a NCMS was created in which the interface between regions with different directions of magnetization does not exceed 10 nm, providing a non-adiabatic regime for the neutron spin transmission through them. NCMS consisted of two magnetic mirrors with magnetization vectors orthogonal to each other and lying in the mirror planes. It was placed in a magnetic field perpendicular to the mirrors. **Figure 7** shows two schemes of experiments to study the behavior of neutrons transmitted through CMS and NCMS. In the first scheme (**Fig. 7**, at the top), the neutron beam was directed in such a way that the sequences "first mirror–magnetic field–second mirror" and "second mirror–magnetic field–first mirror" were realized.

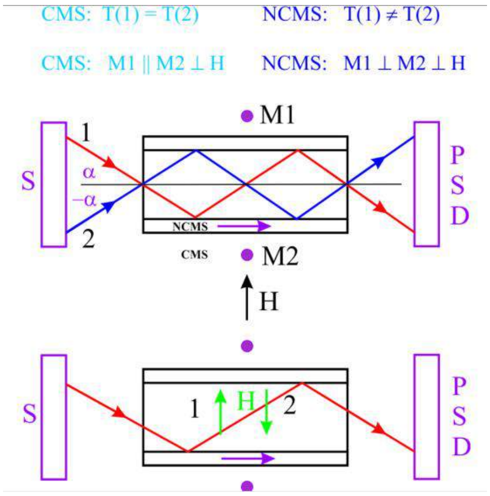

Fig. 7. Schemes of the experiment to verify the dependence of the transmission of unpolarized neutrons on their propagation direction.

Figure 8 shows the neutron intensities for CMS and NCMS, respectively. In the case of NCMS an antiphase behavior of the transmission curves was observed. The second scheme in **Fig. 7** (at the bottom) illustrates the second variant of verification, when the direction of the magnetic field is reversed. In accordance with this scheme **Figure 8** shows the dependences of transmission of unpolarized neutrons for CMS and NCMS, respectively.

Thus, it was shown that the transmission in NCMS depends on the neutron propagation direction, which in its turn is a consequence of non-commutativity of the spin algebra for $S = ½$.

The film coatings based on titanium nitride were studied by neutron and X-ray reflectometry in order to determine the structural parameters (thickness of layers, roughness of the layer interfaces and the scattering length density of individual layers). The monolayer (TiN) and multilayer (TiN/WN) coatings reduce the wear of cutting and shaping tools, increase the surface hardness and reduce the coefficient of friction. The studies were carried out on the neutron reflectometer REFLEX at the IBR-2 reactor and the Bruker X-ray reflectometer at Saint-Petersburg State University. On the basis of the obtained reflection coefficients from the 32-nm-thick film of titanium nitride deposited on a silicon substrate (TiN(32nm)/Si) by magnetron sputtering, the scattering length density (SLD) profiles (DRP) in the direction of the normal to the interface were determined (**Fig. 9**).

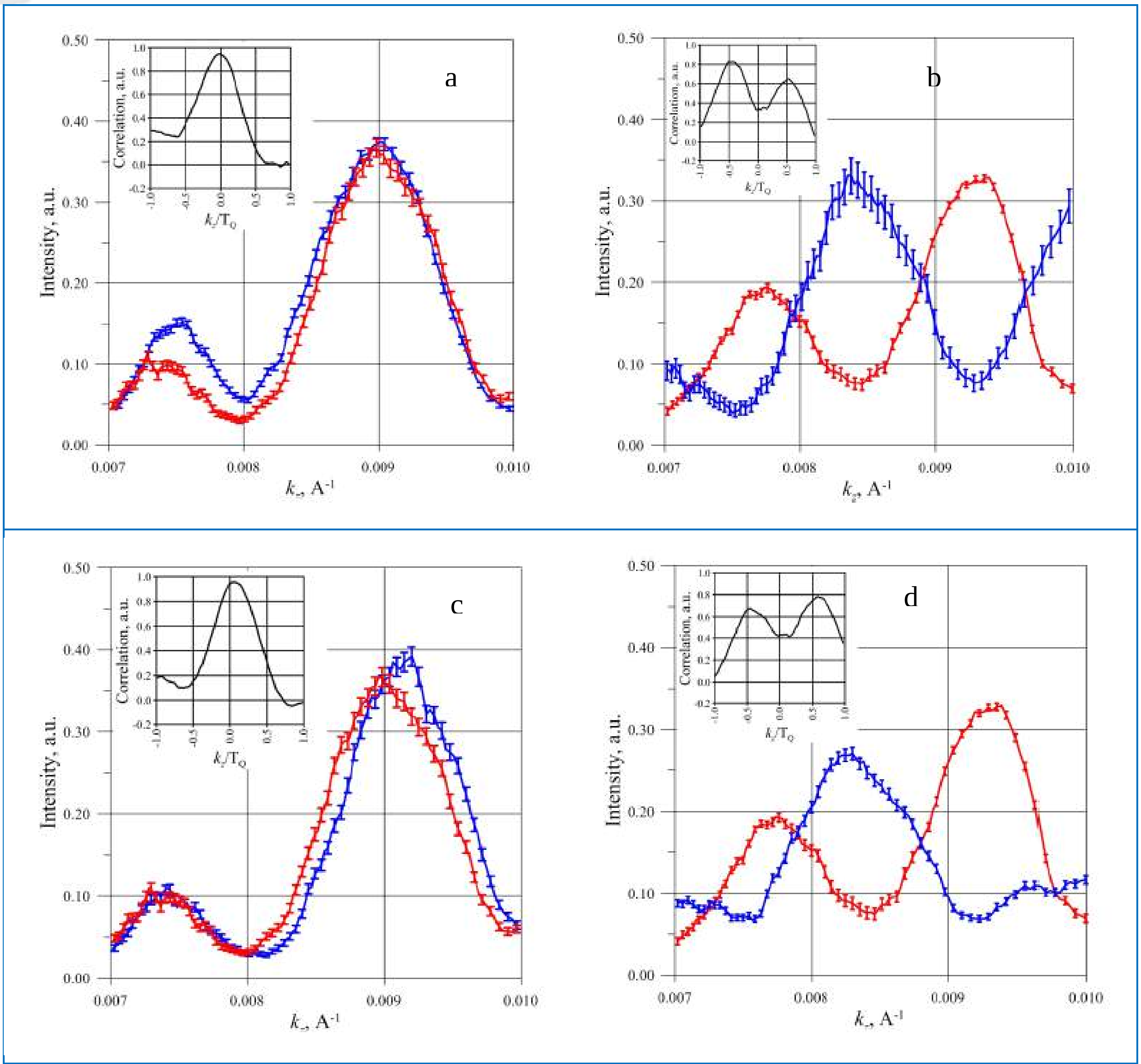

Fig. 8. The transmission for unpolarized neutrons obtained using the first experimental scheme for CMS (a) and NCMS (b). The transmission of unpolarized neutrons obtained by using the second experimental scheme for CMS (c) and NCMS (d).

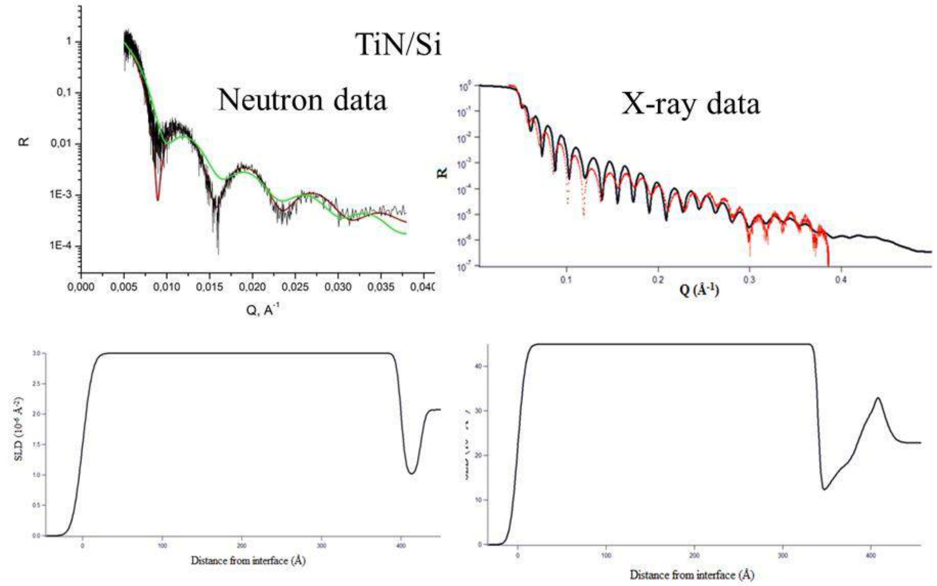

Fig. 9. Neutron (left) and X-ray (right) reflection coefficients from a 36-nm-thick titanium nitride film. The determined scattering length density profiles in both cases (below) show the presence of a transitional layer between the film and the substrate with a relatively low SLD-value. This is indicative of poor adhesion of the film to the substrate surface.

Investigations of biological nanosystems, lipid membranes and complexes

The self-organization and structural parameters of pH-sensitive micelles of surfactants – amine oxides synthesized in the Comenius University (Bratislava, Slovakia) – were studied by small-angle neutron scattering at the Yellow Submarine (Budapest, Hungary) and YuMO instruments. Earlier it has been shown that pH variation provides wide possibilities of controlling properties of specific surfactant molecules – amine oxides. According to the SANS data, at pH < 3 and pH > 8 charged micelles can be observed in solutions, but according to the literature, amine oxides can possess a charge only in acidic media. To obtain more detailed information about the charge, additional studies involving the analysis of ζ-potential in the solutions.

The effect of sucrose on the structure of the lipid bilayer of unilamellar vesicles was studied by small-angle neutron synchrotron radiation scattering [11]. It has been found that when the concentration of sucrose exceeds 40% there is a significant decrease in the thickness of the lipid bilayer.

The model lipid membranes of the lipid matrix of the stratum corneum of the skin were investigated by neutron and X-ray diffraction. The main result obtained is that the superstrong membrane interaction retains after complete membrane hydration.

Polymeric materials

Synthesis and investigation of the structure and physical properties of magnetic elastomers are one of the intensively developing fields of technologies aimed at creating novel "smart" nanomaterials with molecular anisotropy and ferromagnetic nanoparticles. The magnetic elastomers synthesized in the West University of Timisoara, Romania, were investigated by small-angle neutron scattering in the transverse (Pi) and longitudinal (Bi) magnetic fields. Measurements were made on the initial elastomer P1(B1) without ferromagnetic inclusions (matrix) and elastomers P12-P32, P13-

P33, P14-P34 and B2-B4 with ferroparticles of different concentrations polymerized in the absence and presence of an external magnetic field of varying magnitude.

According to the results of neutron studies the initial polymer matrix is anisotropic itself (polymeric clusters of the developed branched chains are more extended in the direction transverse to the film plane). The magnetic field applied in the same transverse direction results in the attraction and convergence of ferroparticles along the field lines. Thus, the polymer is squeezed out of the gaps between the particles, and the polymer cluster anisotropy changes (cluster size increases in the film plane and decreases in the transverse direction). This result was obtained experimentally for the first time and is fully consistent with the results of numerical modeling of the behavior of systems of magnetic particles in an elastic two-dimensional array under magnetization, which point to the positive magnetostriction of structural systems with clusters.

The comparison and analysis of the results describing the glass transition of polymers in the framework of modern theoretical methods were continued. The comparison with the experiment was made on the basis of the data of differential scanning calorimetry for polystyrene at cooling rates in the range from $5 \cdot 10^{-6}$ K/s to 2 K/s. The cooling rate range covered exceeds the available and described in the literature results by three orders of magnitude. It was shown that the use of conventional theoretical methods (TNM, Adam-Gibbs and others) leads to a significant discrepancy with the experiment. A new expression for the relaxation time to describe the experimental data in the framework of the approach with a single order parameter was proposed. The used approaches were compared, and prospects for their further development were analyzed. As additional parameters for comparison, the limiting fictitious temperature of the system, characteristics of the C_p peaks (height and angle) and produced enthalpy were used (**Fig. 10**). The predictive ability of the models was checked using the linear extrapolation of their parameters as a function of the cooling rate. It has been shown that the Adam-Gibbs models give better results [12, 13]. The work was performed in collaboration with the University of Rostock (Rostock, Germany).

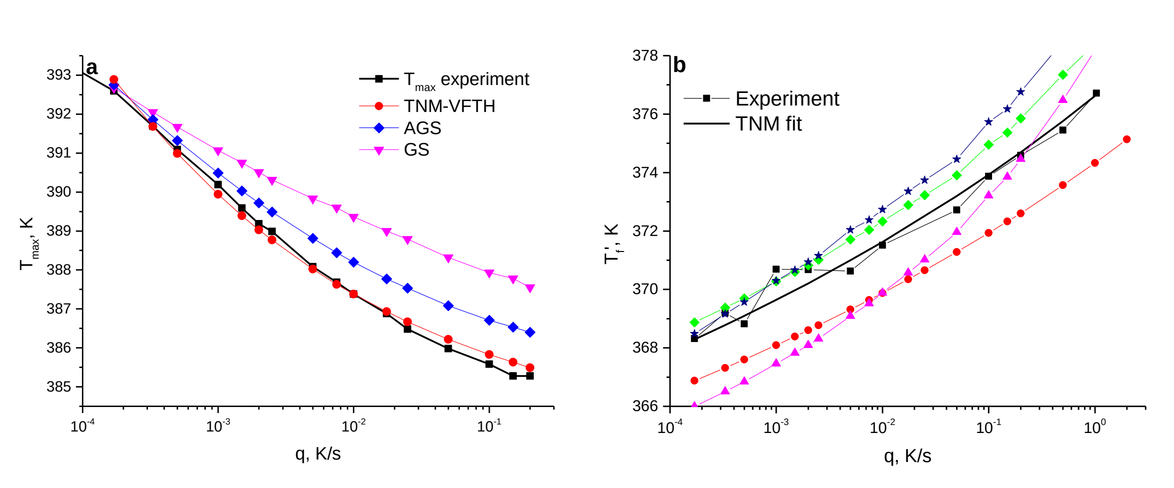

Fig. 10. At the left: Dependence of C_p peak positions on the cooling rate. At the right: Dependence of the experimental and model T_f on the cooling rate. Comparison of different models.

Atomic and molecular dynamics

The vibrational dynamics of water retained in graphene oxide was experimentally and theoretically studied [14]. Nowadays it is generally accepted that graphene oxide (GO) mostly contains hydroxyl (-OH) and epoxy (-O-) groups spread over its basal planes. The presence of hydrogen atoms on the basal planes of freshly synthesized GO sheets points to its metastability. As a result, it transforms into a stable form by a recombination of hydrogen atoms with neighbouring epoxy and hydroxyl groups and produces water, which is always present in graphene oxide materials. The neutron scattering measurements of GO were performed at 20 K on the NERA time-of-flight inverted-geometry spectrometer. The GO sample was synthesized by a modified Hummers method at the Institute of General and Inorganic Chemistry RAS (Moscow). Because of the lack of information on the inelastic scattering spectra for GO we performed the atomistic simulations of the low-temperature spectrum based on the Lerf-Klinowski model with a variable number of water molecules in the interlayer space (with a distance of 7 Å as was revealed in simultaneous measurements by neutron diffraction). In an attempt to simulate the short-range order a systematic periodic model was proposed. Also the calculations using the density functional theory (DFT) were performed. The experimental one-phonon INS spectrum of GO obtained on the NERA spectrometer is compared with the theoretical results and the representative periodic models in **Fig. 11**. There are usually six bands resolved in the experimental spectrum, which were found at about 1500, 1000, 500, 250, 100, and 25 cm^{-1}, respectively. The theoretical calculations allowed us to analyze the specific features of the spectrum. The band in the range of about 1500-1200 cm^{-1} can be accurately attributed to the set of δC-O-H modes. The dominant and pronounced feature covering the range of ~ 700-300 cm^{-1} may be linked with the set of libration modes of water. The general shape and position of this band were properly restored. The libration modes are widely distributed below 700 cm^{-1} in the following order: $\omega H^{-}O\text{-}H > \tau H^{-}O\text{-}H > \rho H^{-}O\text{-}H$.

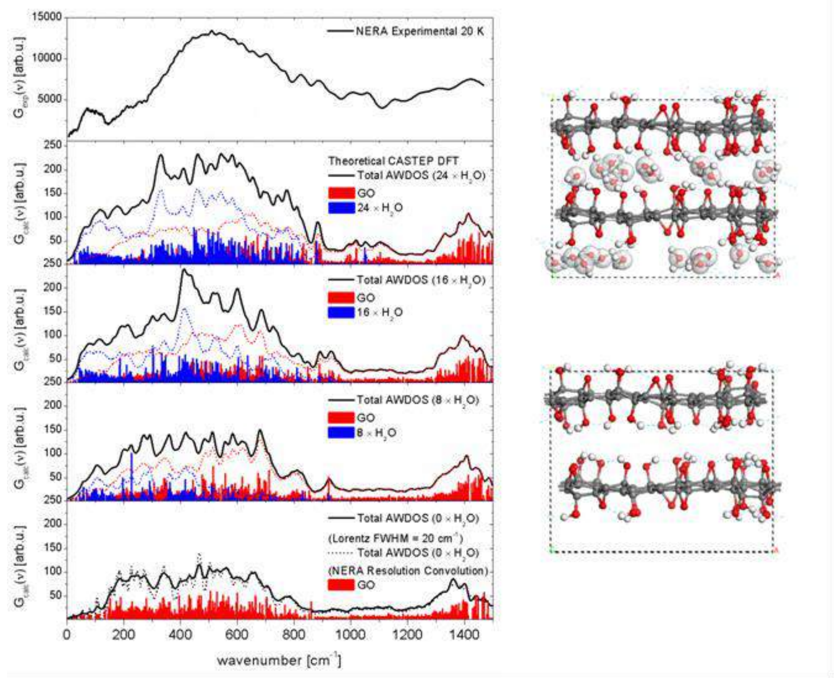

Fig. 11. Spectra of amplitude-weighted density of vibrational states (AWDOS) for graphene oxide calculated by means of periodic DFT calculations obtained by varying the number of interlayer water molecules. The representative molecular models (non-solvated and including 24 H_2O molecules) are also shown.

The wagging modes, as a rule, manifest themselves in the range of > 600 cm^{-1}, whereas the twisting modes are located at < 600 cm^{-1}. The vibrational modes are widely spread below 500 cm^{-1}. The experimental bands arising at ~250 cm^{-1} and ~50-150 cm^{-1}, respectively, can be associated with the translational modes of coordinated water. According to the calculations, the upper band can be attributed mainly to $\nu O\cdots O$ stretching vibrations of water molecules hydrogen-bonded with hydroxyl groups. The band around ~ 50-150 cm^{-1} may be linked with the visible motions of the centers of masses of water, which are, in turn, strongly coupled with the deformations of the GO structure. The modes formed below 100 cm^{-1} can be attributed to the water transitional modes strongly coupled with the butterfly-like deformations of the GO layers. Finaly, the energetically lowest modes were theoretically found at about 30 and 45 cm^{-1}, respectively. The upper modes can be associated with the so-called 'breathing' motions of the GO framework; which may be described as a fluctuation of the interlayer distance. The lowest vibrations (so-called shearing modes) correspond to the parallel translations of the layers. These motions show up as a band observed experimentally at 30 cm^{-1}. The analysis allowed a satisfactory qualitative description of the corresponding inelastic scattering spectrum (determined mainly by the interlayer water molecules), which confirms the correctness of the Lerf-Klinowski model.

On the DIN-2PI spectrometer the inelastic coherent neutron scattering from liquid gallium was investigated at an initial neutron energy E_o = 28.7 meV and 7.65 meV and sample temperatures T = 333 K and 533 K (**Fig. 12**). It was found that the dispersion curve in liquid gallium splits into two branches, which is, apparently, due to the presence of two types (metallic and covalent bonding) of particle interaction in this metal. This feature of the particle interaction in gallium is also reflected in the structure of the liquid metal as the asymmetry of the main peak of its structure factor.

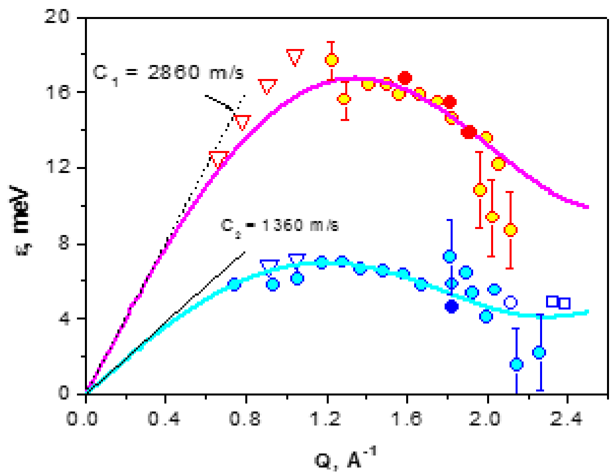

Fig. 12. Dispersion curves in liquid gallium (T = 333 K). The circles show the experimental data obtained on the DIN-2PI spectrometer (open circles – initial neutron energy E_0 = 28.7 meV, full circles – E_0 = 7.65 meV). Open squares show inelastic neutron scattering. Triangles – inelastic scattering of synchrotron radiation. C1 and C2 denote sound velocities for the top and bottom branches of the dispersion curve.

Applied research

Among traditional applied investigations in the NICM Department are the experimental studies of internal stresses and texture of rocks and minerals, determination of internal stresses in bulk materials and products, including engineering materials and components of machines and devices. For the most part, these investigations are carried out using neutron diffraction.

On the FSD diffractometer the experiments on investigations of residual stress distributions in welded joints obtained by various methods of beam welding were continued [15] (**Fig. 13**). Samples for measurements were produced in the Institute of Electronics, BAS (Sofia, Bulgaria) in the form of plates welded by electron-beam (EBW) and laser-beam (LBW) welding. It was found that the residual stress maxima are located not in the centers of the welds, but in a heat-affected zone (HAZ), and the residual stress level decreases rather sharply in regions remote from HAZ. Maximum-largest in both samples is the component of the stress tensor σ_x directed along the weld line and having mainly stretching character. For EBW and LBW samples maximum levels of residual stresses are comparable in magnitude and reach values of 460 and 530 MPa, respectively. Basing on the results of the previous experiments at FSD on residual stresses in witness specimens from nuclear power plants, it may be noted that the stress level in the specimen LBW is typically high for this type of welding. At the same time, the EBW sample demonstrates a substantially greater level of stresses in comparison with that achieved for witness specimens with electron-beam welding (~ 200 MPa). The results of these measurements point to non-optimal parameters of the electron-beam welding, and, thus, there is a possibility for their improvement and residual stress reduction. Along with it, the results of neutron measurements can serve as a reliable method for diagnostics of the residual stress level.

In addition to the study of residual stresses in these samples, the residual microstrains (**Fig. 13**) were investigated as well. They were derived from the broadening of the diffraction peaks against the instrumental resolution function. The analysis of the behavior of the widths as a function of the interplanar spacing d_{hkl} has shown that the peak broadening is anisotropic and depends on the direction [hkl] in the crystal. This behavior is a typical manifestation of the orientation factor of dislocations in respect to the scattering vector, which allows one to quantitatively assess the density of dislocations in a material under study. In the EBW sample the maximum level of microstrains in the material reaches $2.5 \cdot 10^{-3}$, and the positions of the maxima in the microstrain distribution are in good agreement with the locations of the weld centers. In the LBW sample the maximum level of microstrains is almost twice as high, $4.5 \cdot 10^{-3}$. The obtained experimental data will be used for further model calculations by the finite element method (group of Prof. V.Mikhailov, Brandenburg University of Technology, Germany) and compared with the results of mechanical tests by drilling holes, microhardness measurements and optical studies of the microstructure (group of Prof. P.Petrov, Institute of Electronics BAS, Bulgaria).

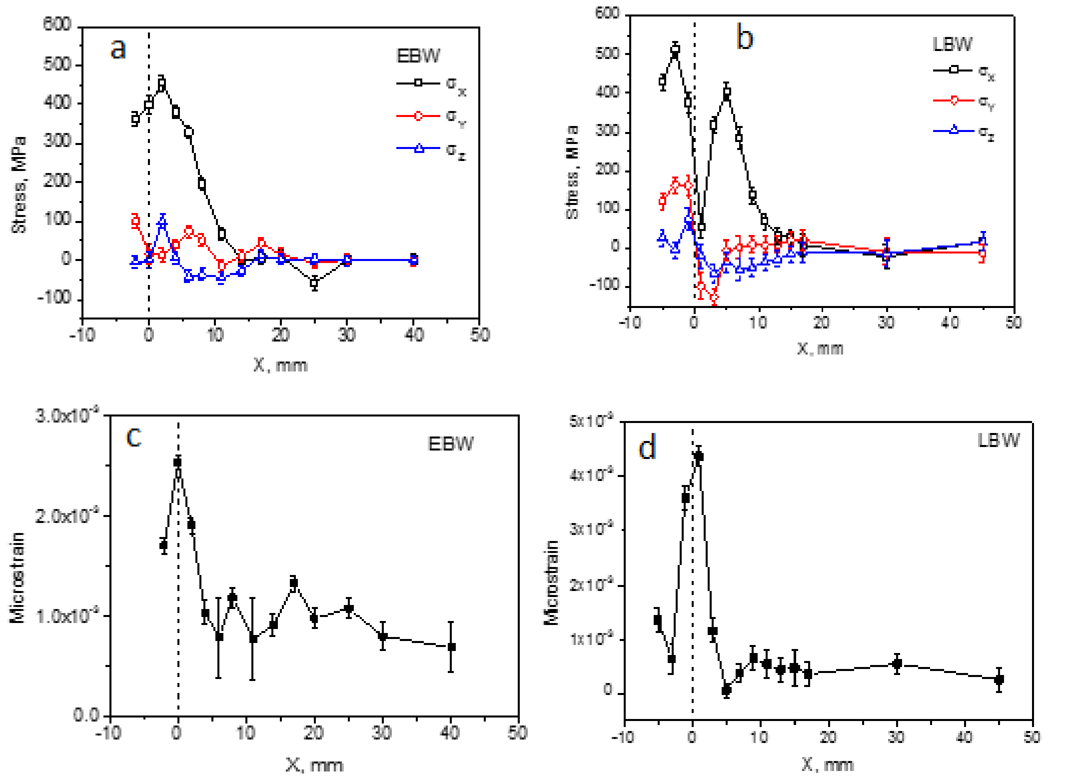

Fig. 13. Residual stress distribution in an S355J2+N steel plate welded by EBW (a) and LBW (b) welding. Residual microstrain distribution in an S355J2+N steel plate welded by EBW (c) and LBW (d) welding.

This will make it possible to study systematically the dependence of the residual stress distribution on the used technology in the welding process and on its parameters for the most widely used engineering materials. Thus, this information can serve as a basis for developing specific technical recommendations to achieve the desired level and profile of residual stresses.

The texture, inner stresses, and stresses under applied load in multiphase polycrystalline samples of granite [16] were studied at diffractometers SKAT and Epsilon (**Fig. 14**). The experiments to study mechanical properties under uniaxial cyclic deformation were carried out in a load range up to 100 kN (150 MPa) and supplemented by a simultaneous acoustic emission analysis.

The obtained values for the inner stresses ranged from -1×10^{-3} to 1.2×10^{-3}. When measuring stresses under the applied load, the z-axis of the cylindrical sample was oriented at an angle of 45° relative to the neutron beam, allowing the simultaneous measurement of components σ_1 and σ_3. The negative stresses along the z-axis are consistent with the Hooke's law, the positive stresses along the x-axis oriented perpendicular to σ_3 are smaller and determined by the Poisson's ratio.

In cooperation with the O.Honchar Dnepropetrovsk National University (Ukraine) a number of samples of ferrite-pearlite wheel steel R7 were studied to determine the effect of modification and thermo-mechanical treatment on the crystallographic texture [17]. The samples were cut out of the rail wheel rims and the transitional zone (between the wheel hub and disk). The texture measurements were carried out using the thermal neutron diffraction technique on the SKAT diffractometer. Three complete pole figures (PF) (200), (110), (211) for α-Fe phase in 5˚×5˚grid were extracted from a set of 1368 (19×72) measured spectra for each sample.

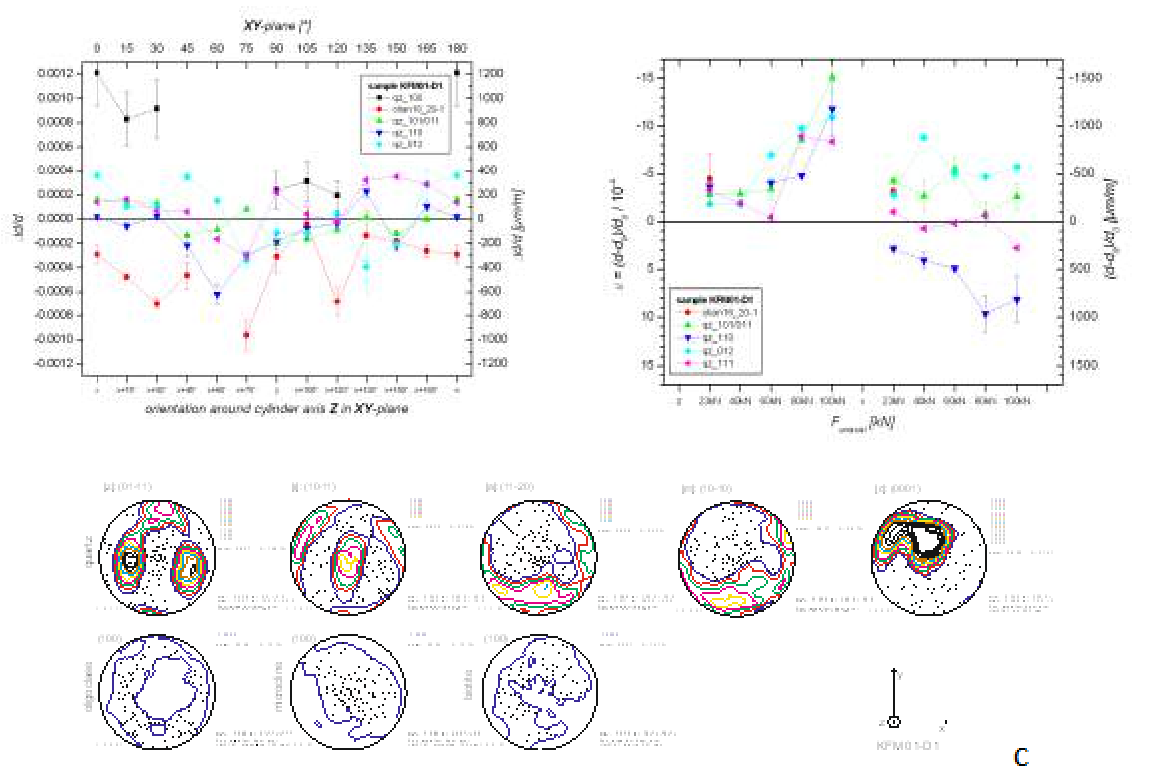

Fig. 14. (a) Inner stresses for crystallographic planes of quartz (10-10), (10-11)/(01-11), (11-20), (01-12), 11-21) and oligoclase (20-1). (b) Stresses under the action of the applied load for crystallographic planes of quartz (10-10), (10-11)/(01-11), (11-20), (01-12), 11-21 and oligoclase (20-1). c) Pole figures characterizing the texture of quartz, oligoclase, microcline and biotite.

1. SCIENTIFIC RESEARCH

Using the measurement data, the texture components of the deformation and recrystallization corresponding to the technological procedures in the wheel manufacturing process were determined even for very weak textures. It has been concluded that for the samples from the rim the introduction of a modifier in the alloy causes a change in the weak preferred orientation. The reorientation of the texture component during annealing can be explained by secondary recrystallization processes and phase transitions in steel. The changes in the scattering of the texture components in the modified samples are associated with the introduction of the modifier as well as with some differences in the heat treatment modes that were applied to the experimental and conventional steels. Despite the weak character of the texture, the rolling texture components (Δ symbols in Fig. 15) and recrystallization components (• symbols in Fig. 15), characteristic for bcc structure materials, were determined, which confirms the high potential of the SKAT diffractometer (**Fig. 15).**

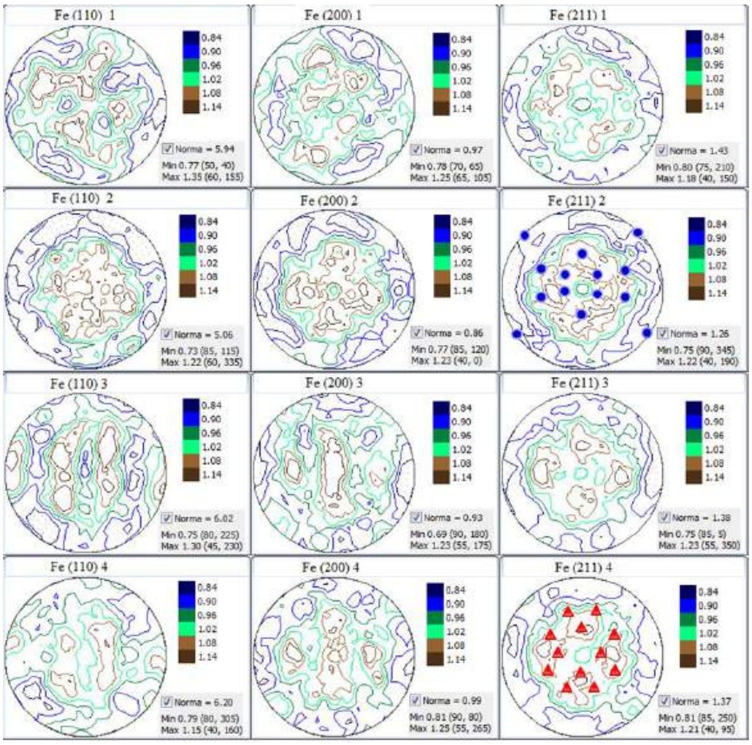

Fig. 15. Changes in the crystallographic texture in the modified samples of wheel steel after heat treatment. Pole figures for α-Fe (110), α-Fe (200) and α-Fe (211) are shown.

II. Instrument development

Work to develop the final configuration of the new DN-6 diffractometer was carried out. In cooperation with the SC Department the construction of a second ring-shaped detector consisting of 96 independent helium counters is in progress. The first successful methodological experiments on neutron diffraction in diamond anvil cells with Fe_3O_4 magnetite samples were conducted at pressures of up to 23 GPa (**Fig. 16**). Also, work was carried out on further development of the technique of the neutron experiment using high-pressure sapphire anvil cells. The accessible pressure range was extended up to 12 GPa by reducing the working area of the anvils down to 1 mm.

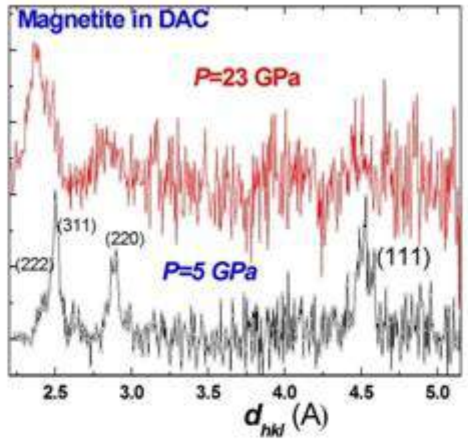

Fig. 16. Neutron diffraction spectra of Fe_3O_4 magnetite obtained using diamond anvil cells at the DN-6 diffractometer at pressures of 5 and 23 GPa.

In 2014, work was carried out on the preparation of the GRAINS reflectometer for operation within the framework of the user policy program. The GRAINS reflectometer was included in the list of facilities available to the IBR-2 users, and the description of the setup was posted on the FLNP website. Specialized liquid cells (**Fig. 17**) were developed and tested for studying liquid/air and liquid/solid interfaces. A universal holder for performing measurements with solid samples was created. An automatic movable platform for the detector (**Fig. 17**) was installed in its working place and tested. In the framework of the development of new coatings for neutron optical devices the experiments were performed to study the oxidation effect on the structure of thin films on glass substrates.

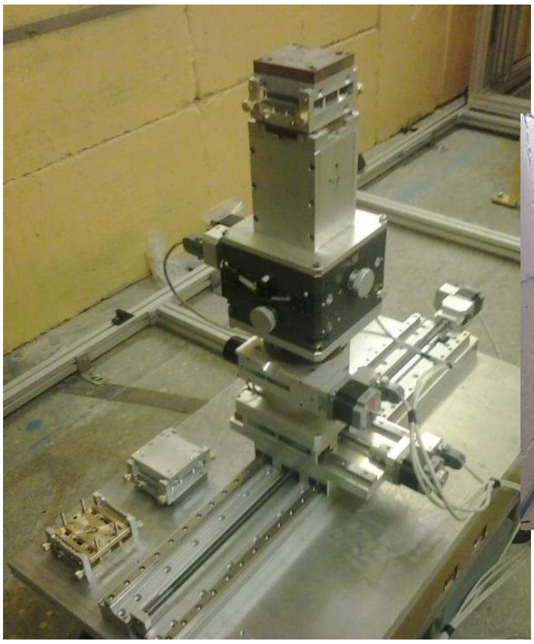

Fig. 17. Sample table with a liquid cell (left) and automatic movable platform for the detector (right).

The implementation of the project aimed at constructing a new diffractometer on beamline 6a for neutron diffraction studies of transition processes in real time was continued. A background shield was manufactured and installed for the diffractometer detector system (ring-shaped detector in the axial geometry for backscattering angles, two modules comprising eight point counters for medium scattering angles and a module consisting of eight counters for small scattering angles). New preamplifiers were installed on the point detectors. A thermostat covering a temperature range from –40°C to +100°C was put into service and first measurements with model biological membranes were carried out.

The development of a prototype of the spectrometer for neutron radiography and tomography on beamline 14 (**Fig. 18**) continued. A HUBER goniometer with translational and rotational degrees of freedom was installed in working position. First tomography experiments with different types of objects were conducted (**Fig. 19**). The procedure of 3D-reconstruction of the internal structure of objects using a variety of software packages was optimized. The obtained results showed a good quality of the acquired data which is comparable to that achieved in other world neutron centers.

Fig. 18. Spectrometer for neutron radiography and tomography on IBR-2 beamline 14.

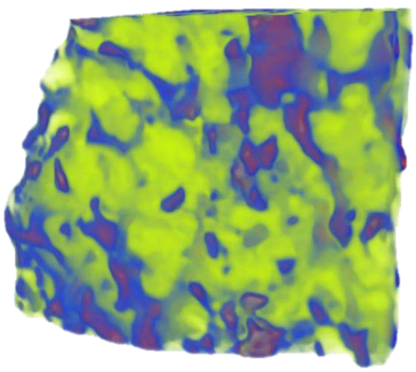

Fig. 19. Neutron tomographic image of the meteorite Seymchan showing the distribution of Fe-Ni alloy and fraction of rocks (mainly olivine).

In 2014, the 4-th element (out of 7 planned) of ZnS-based 90°-detector ASTRA_Right with wavelength-shifting optical fiber readout was installed on FSD in cooperation with the specialists from the SC Department. By the end of 2014 the final geometric alignment of this element on FSD and adjustment of operating parameters of the detector are to be performed. Thus, the continuation of work on the extension of the multi-element detector system of FSD will significantly enhance the detector solid angle.

The work was continued on the introduction of list-mode data acquisition electronics into regular operation. In 2014, at the FSD diffractometer during the experiments in cycles №6 (October, water moderator mode) and №7 (November, cryogenic moderator mode) the list-mode analyzer was tested in the regime of real continuous operation. The comparative analysis of spectra recorded in parallel by the "old" and new list-mode analyzer has shown their identity. In addition, the acquisition of data from all elements of 90°-detectors ASTRA with the subsequent application of electron focusing made it possible to enhance the efficiency of the experiment by a factor of 3.

A new analyzer was also installed on HRFD and first experiments were conducted with comparative simultaneous measurement of diffraction spectra using the existing DSP-based analyzer and the new list-mode analyzer. High-resolution spectra were extracted from the list-mode data using the developed algorithm and compared with the DSP-spectra. The comparison has shown that the spectra are identical (**Fig. 20**), which is indicative of the correct operation of the new electronics and the developed algorithms for obtaining diffraction spectra from "raw" data. The problem that needs to be solved is insufficient data processing speed at the available computation power. At present, the equipment is being purchased and algorithms are being developed, which will allow an increase in the processing speed of at least ~100 times.

On IBR-2 beamline 13 the development of the Fourier diffractometer FSS was continued in cooperation with the SC Department. In 2014, the design study for the installation of the diffractometer was completed. At present, the construction of biological shielding and installation of necessary technological equipment have mainly been completed. In addition, on FSS a steel collimator was installed in the embedded tube of the beamline to reduce the radiation load on the neutron guide; 1st section of the mirror neutron guide and a Fourier-chopper with a table were assembled and installed.

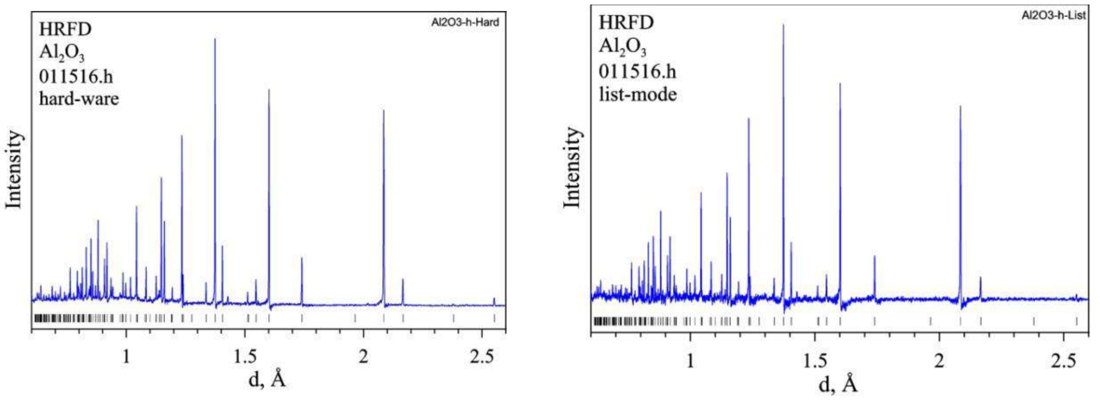

Fig. 20. Comparison of the diffraction spectra measured on HRFD using DSP-analyzer (left) and list-mode-analyzer (right). One can see the similarity of the spectra and identical relative intensities of the diffraction peaks. Slightly enhanced background in the case of the list-mode analyzer is connected with non-optimal (increased) strobe pulse width.

For the REMUR reflectometer a sample module for experiments in an alternating magnetic field with a frequency of 10-60 MHz and a magnetic system of a wide-aperture polarization analyzer designed for operating with a two-dimensional PSD (**Fig. 21**) were manufactured.

Fig. 21. A sample module for experiments in an alternating magnetic field with a frequency of 10-60 MHz (left) and a magnetic system of a wide-aperture polarization analyzer (right) of the REMUR reflectometer.

In order to evaluate the possibilities of different methods of microstructural characterization based on the analysis of data obtained at the HRFD TOF-diffractometer, the experiments with a set of niobium carbide NbC_y powders, y ≈ 0.93 (cubic lattice), with various mean crystallite sizes in a range of 100-2500 Å, were performed [18]. The additional experiments were carried out on the HRPT high-resolution diffractometer with a monochromatic neutron beam in PSI (Switzerland). The combined data analysis was performed using the classical Rietveld and Williamson-Hall methods and with the application of the Whole Powder Pattern Modeling (WPPM) technique. The samples of niobium carbide $NbC_{0.93}$ with different mean crystallite sizes were obtained by high-energy milling of an initial coarse grain powder during various periods of time, which are indicated in the sample names as NbC-n, where n = 0, 1, 5, 10, 15 is the milling time in hours. Some powder diffraction spectra of NbC-n measured on HRFD are shown in **Fig. 22**. The treatment of the diffraction spectra of the milled samples by the Rietveld method revealed the presence of two fractions with very different widths of the peaks and biased peak maxima. In the analysis of the widths of the diffraction peaks the classical Williamson-Hall method was used which implies the analysis of the dependence of "half-width" (full width at half maximum, FWHM) or integral peak widths as a function of a scanned variable in the diffraction spectra.

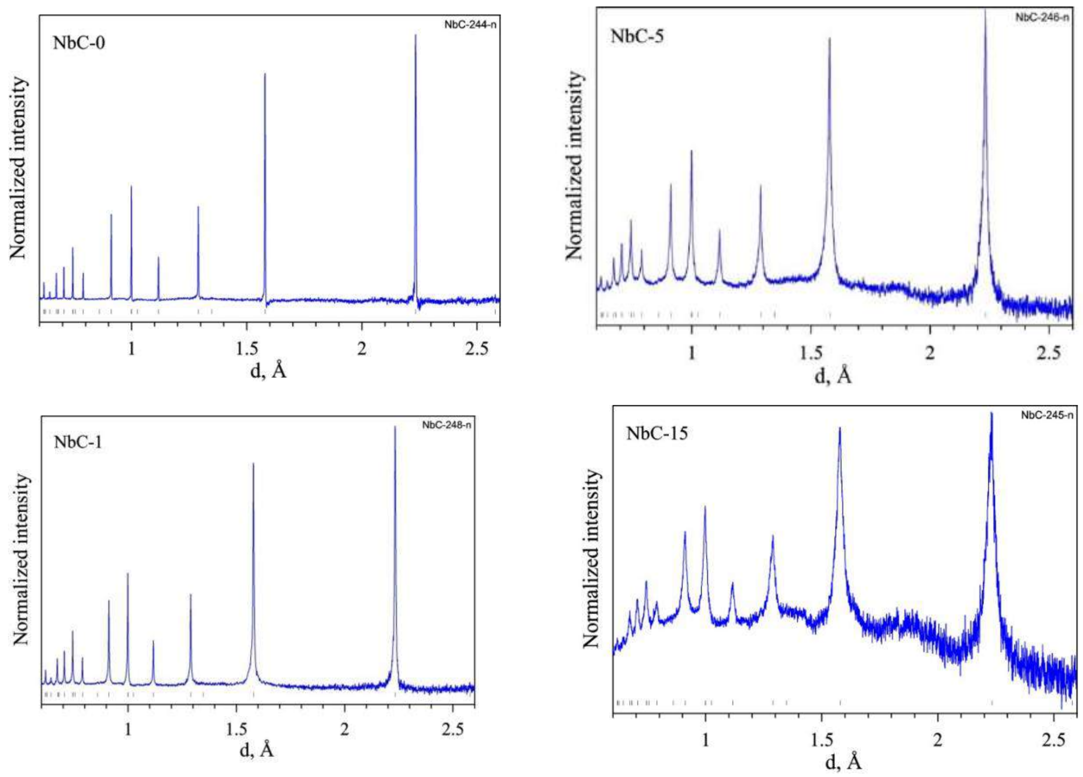

Fig. 22. Normalized powder diffraction spectra of NbC-n, n = 0, 1, 5, 15 measured at HRFD. The peak width and the incoherent background increase with increasing milling time. After 5- and 15-hour milling a broad peak at d ≈ 1.9 Å appears, which is associated with the formation of an amorphous phase and the formation of a low order in it. The vertical lines show the calculated peak positions.

The dependence $W^2(d^2)$ for the initial powder NbC-0 is shown in **Fig. 23**, where the contribution of the HRFD resolution function to the peak width is given as well. For polycrystalline powders NAC and Al_2O_3 this dependence is linear, whereas the experimental points for NbC-0 is better described by a parabola, which corresponds to L ≈ 2550 Å. The main difference of this depenedence for NbC-0 from the resolution function is associated with the presence in the powder of microstrains at a level of $\varepsilon \approx 1\cdot10^{-3}$. The same dependence for the milled powders showed that the experimental data cannot be described by a single curve, since there is a significant scatter of the experimental points. This effect can be attributed to the manifestation of the strong microstrain anisotropy, i.e. the dependence of the peak broadening on a specific set of Miller indices.

The implementation of the WPPM method in the PM2K software package allows one to process neutron data from a diffractometer with a monochromatic beam. Spectra obtained on a TOF-diffractometer including HRFD can be processed but without regard for correct weights of experimental intensities. Nevertheless, PM2K was probed in the analysis of the data for powders NbC-0 and NbC-10 which were obtained on HRFD and HRPT. When calculating the profiles of the diffraction peaks the crystallite size distribution and the presence of some dislocation density were taken into account in addition to the resolution function effect. The size distribution of the lognormal type was used. For NbC-0 the calculated mean crystallite size, $\langle L \rangle_V$ = 2230 Å, is close to the value of L = 2550 Å determined by the Williamson-Hall method. For the NbC-10 powder the values $\langle L \rangle_V$ = 169 Å and 142 Å were obtained according to the HRPT and HRFD data, respectively; the corresponding lognormal distributions are shown in **Fig. 22**. This means that the processing of HRFD data even without considering correct weights allows one to obtain reasonable results.

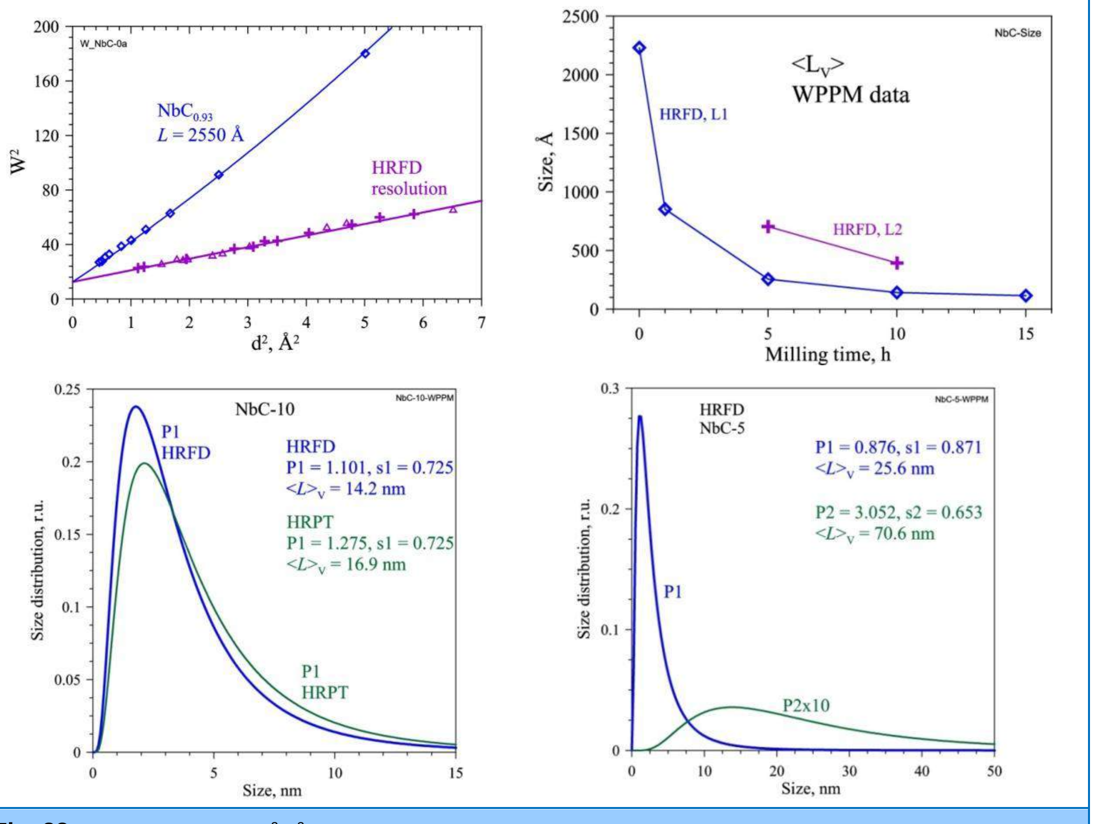

Fig. 23. (a). Dependence $W^2(d^2)$ for the initial powder NbC-0 (blue diamonds) and contribution to the peak width of the resolution function of HRFD (bottom line) determined from the spectra of standard powders NAC and Al_2O_3 (crosses and triangles). Dependences $W^2(d^2)$ for NAC and Al_2O_3 are linear, which is indicative of the fact that there is no size effect. The size effect (L ≈ 2550 Å) manisfests itself in the dependence for NbC-0. (b) The milling time dependence for characteristic crystallite sizes (regions of coherent scattering) obtained by the WPPM method for the F1 fraction (all samples) and F2 fraction (NbC-5 and NbC-10). (c) The log-normal size distribution of crystallites in the main phase for NbC-10, calculated from the diffraction data obtained on HRFD and HRPT. The diffraction sizes are 14 and 17 nm, respectively. (d) The log-normal size distribution of crystallites in NbC-5 obtained from the diffraction data measured on HRFD. Two fractions with different distribution parameters corresponding to the diffraction sizes of 256 Å and 706 Å are determined

On the REFLEX reflectometer the influence of an oxide layer in titanium films covering polarizing supermirrors on their polarizing efficiency was investigated (**Fig. 24**). The top layer of titanium is designed to protect the layers of cobalt and iron (the basis of supermirrors) from oxidation. Along with it, an oxide layer with an approximately zero SLD forms on the very titanium film. Thus, the titanium oxide layer has not only a protective function, but becomes practically transparent to thermal neutrons without impairing the reflective properties of the supermirror. On the REFLEX reflectometer the reflection coefficients for two neutron spin states were measured for a series of samples with different thicknesses of the oxide layer. The experimental results are currently being processed; the corresponding publication is under preparation.

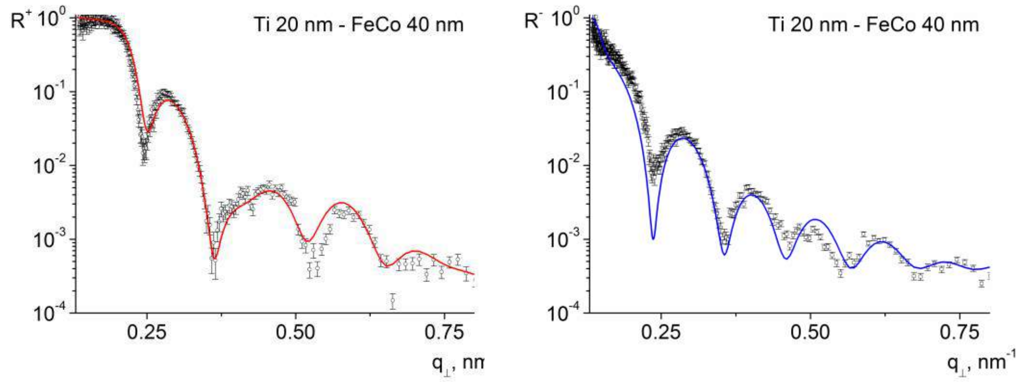

Fig. 24. Reflection coefficients of polarizing films coated with a titanium oxide layer for two neutron spin components.

The simulation of experiments on spin-echo small-angle scattering from perfect uniform spheres a few tens of nanometers in diameter was performed using the VITESS software package. The scheme of the spin-echo spectrometer implemented in the VITESS package corresponded to the spin-echo instrument on beamline 9 of the IBR-2 reactor. The scattering curves obtained from the Monte Carlo simulations are in satisfactory agreement with the theoretical calculations (**Fig. 25**).

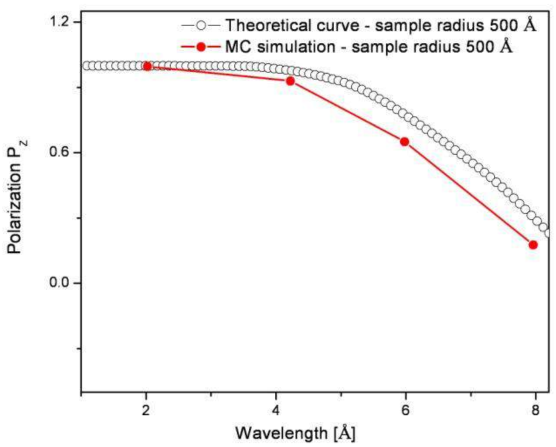

Fig. 25. Dependence of the neutron beam polarization after passing the second arm of the spin-echo spectrometer in scattering by perfect spheres 50 nm in diameter. The red curve corresponds to theoretical calculations, the black one shows the results of the Monte Carlo simulation of the experiment in the VITESS package.

On the REMUR reflectometer the experiments to obtain a set of neutron microbeams with different wavelengths and intensity distribution over the scattering angle for the resonances n = 0, 1, 2 at the grazing angles of the incident beam of 2.55, 3.27, 5.82 and 6.92 mrad were performed

(**Fig. 26**). A three-layer structure (planar waveguide) converts a conventional collimated neutron beam about 0.1 mm into a narrow divergent neutron microbeam about 0.1 μm wide. Such a narrow probe makes it possible to scan local microstructures with high spatial resolution. Neutrons fall on to the surface of the film, penetrate the waveguide layer, propagate along the film in the waveguide layer (channelling) and come out of the end side as a narrow strip. The divergence of the microbeam in this case is determined by the conditions of Fraunhofer diffraction from a narrow slit. Inside the waveguide one can observe the phenomenon of resonant amplification of neutron density followed by the generation of neutron standing waves. Therefore, the microbeam at the output of the waveguide has a narrow wavelength distribution around the resonant wavelength. At steady-state neutron sources the wavelength is fixed and limited to the value of about 4 Å, and at pulsed sources the wavelength of the microbeam can be changed by varying the grazing angle of the incident beam. The obtained experimental data are in agreement with the theoretical predictions. Using the time-of-flight method the waveguide can be easily tuned to any required wavelength of the microbeam including wavelengths above 4 Å. And by selecting certain intervals of the scattering angle one can simultaneously register several microbeams.

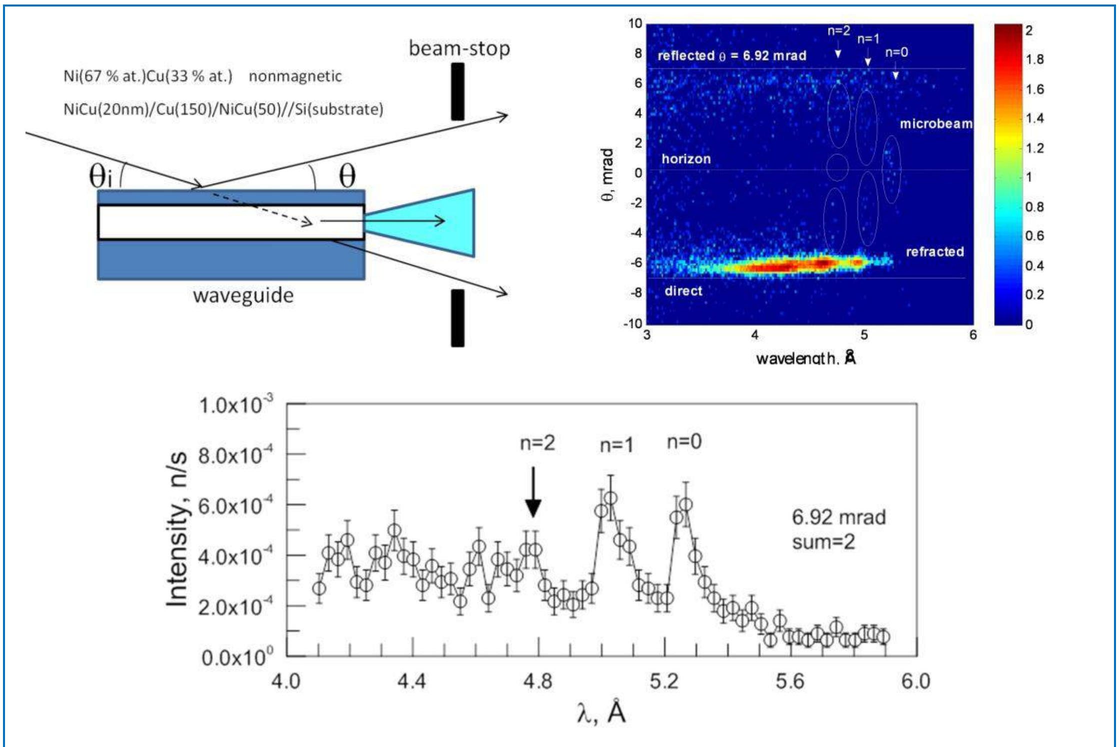

Fig. 26. Scheme of the experiment to obtain neutron microbeams (a). Distribution of scattered neutron intensity over the scattering angle and wavelength (b, c).

References

1. Kozlenko D.P., Kichanov S. E., Lukin E. V., Dang N. T., Dubrovinsky L. S., Liermann H.-P., Morgenroth W., Kamynin A. A., Gridnev S. A., Savenko B. N., Pressure-induced polar phases in relaxor multiferroic $PbFe_{0.5}Nb_{0.5}O_3$. (2014) Physical Review B, v. 89, p. 174107 (1-7).

2. Burzo E., Vlaic P., Kozlenko D.P., Kichanov S.E., Dang N.T., Rutkauskas A.V., Savenko B.N., Magnetic properties, electronic structures and pressure effects of $Ho_xY_{1-x}Co_2$ compounds. (2014) Journal of Alloys and Compounds, v. 584, pp. 393–401.

3. Kozlenko D.P., Burzo E., Vlaic P., Kichanov S.E., Rutkauskas A.V., Savenko B.N., Sequential Cobalt Magnetization Collapse in $ErCo_2$: Beyond the Limits of Itinerant Electron Metamagnetism. (2014) Scientific Reports, in consideration.

4. Melníková L. , Petrenko V.I. , Avdeev M.V. , Garamus V.M. , Almásy L., Ivankov O.I. , Bulavin L.A. , Mitróová Z., Kopčanský P., Effect of iron oxide loading on magnetoferritin structure in solution as revealed by SAXS and SANS. (2014) Colloids and Surfaces B, in press.

5. Kopcansky P., Siposova K., Melnikova L., Bednarikova Z., Timko M., Mitroova Z., Antosova A., Garamus V.M., Petrenko V.I., Avdeev M.V., Gazova Z., Destroying activity of magnetoferritin on lysozyme amyloid fibrils. (2014) Journal of Magnetism and Magnetic Materials, in press.

6. Melnikova L., Petrenko V.I., Avdeev M.V., Ivankov O.I., Bulavin L.A., Garamus V.M., Almásy L., Mitroova Z., Kopcansky P., SANS contrast variation study of magnetoferritin structure at various iron loading. (2014), Journal of Magnetism and Magnetic Materials in press.

7. Petrenko V.I., Avdeev M.V., Garamus V.M., Bulavin L.A., Kopcansky P., Impact of polyethylene glycol on aqueous micellar solutions of sodium oleate studied by small-angle neutron scattering. (2014) Colloids and Surfaces A, accepted.

8. Prylutskyy Yu.I., Petrenko V.I., Ivankov O.I., Kyzyma O.A., Bulavin L.A., Litsis O.O., Evstigneev M.P., Cherepanov V.V., Naumovets A.G., Ritter U.. On the origin of C60 fullerene solubility in aqueous solution. (2014) Langmuir v.30, p. 3967−3970.

9. Tomchuk O.V., Bulavin L.A., Aksenov V.L., Garamus V.M., Ivankov O.I., Vul’ A.Ya., Dideikin A.T., Avdeev M.V., Small-angle scattering from polydisperse particles with a diffusive surface.(2014) Journal of Applied Crystallography, v.47, p.642–653.

10. Tatarskiy D.A., Petrenko A.V., Vdovichev S.N., Udalov O.G., Nikitenko Yu.V., Fraerman A.A., Nonreciprocal transmission of neutrons through the noncoplanar magnetic system. (2014) Physical Review Letter, submitted.

11. Киселев М.А., Земляная Е.В., Жабицкая Е.И., Аксенов В.Л., Исследование однослойных везикул ДМФХ в водных растворах сахарозы методами малоуглового рассеяния нейтронов и рентгеновских лучей. (2015) Кристаллография, т. 60, №1, с.140-150.

12. Schmelzer J.W.P., Tropin T.V., Kinetic criteria of glass-formation, pressure dependence of the glass-transition temperature, and the Prigogine-Defay ratio. (2014)Journal of Non-Crystalline Solids, (in press).

13. Tropin T.V., Schulz G., Schmelzer J.W.P., Schick C., Heat ca pacity measurements and modeling of polystyrene glass transition in a wide range of cooling rates. (2014) Journal of Non-Crystalline Solids, (in press).

14. Drużbicki K., Natkaniec I., Vibrational Properties of Water Retained in Graphene Oxide. (2014) Chemical Physics Letters, v. 600, p.106–111.

15. Bokuchava G.D., Papushkin I.V., Petrov P.I., Residual Stress Study by Neutron Diffraction in the Charpy Specimens Reconstructed by Various Welding Methods. (2014) Comptes rendus de l'Académie Bulgare des Sciences, v. 67, p. 763-768.

16. Scheffzuek C., Ullemeyer K., Vasin R., Naumann R., Schilling F.R. Strain and texture investigations by means of neutron time-of-flight diffraction: application to polyphase gneisses. (2014) In: Holden T.M., Muránsky O. & Hamelin C.J. (Eds.): Mechanical Stress Evaluation by

Neutrons and Synchrotron Radiation VII. Materials Science Forum v. 777, p. 136-141.

17. Lychagina T., Nikolayev D., Sanin A., Tatarko J., Ullemeyer K., Investigation of wheel steel crystallographic texture changes due to modification and thermo-mechanical treatment. (2014) Materials Science and Engineering, Dresden.

18. Курлов А.С., Бобриков И.А., Балагуров А.М., Гусев А.И., Анизотропия деформационных искажений в нанокристаллических порошках нестехиометрического карбида ниобия $NbC_{0.93.}$ (2014) Письма в ЖЭТФ, т. 100,(в печати).